Inorganic Chemistry

pubs.acs.org/IC

Article

Magnetic Phase Separation in the Oxypnictide $Sr_2Cr_{1.85}Mn_{1.15}As_2O_2$

Bor Arah, Clemens Ritter, Gavin B. G. Stenning, and Abbie C. Mclaughlin*

Cite This: *Inorg. Chem.* 2022, 61, 12518−12525

Read Online

ACCESS | Metrics & More | Article Recommendations | Supporting Information

ABSTRACT: Layered $Sr_2M_3As_2O_2$-type oxypnictides are composed of tetrahedral M_2Pn_2 and square planar MO_2 layers, the building blocks of iron-based and cuprate superconductors. To further expand our understanding of the chemical and magnetic properties of the $Sr_2Cr_{3-x}Mn_xAs_2O_2$ solid solution, $Sr_2Cr_2MnAs_2O_2$ has been synthesized. The compound crystallizes in the *I*4/*mmm* tetragonal space group with a refined stoichiometry of $Sr_2Cr_{1.85}Mn_{1.15}As_2O_2$. The M(2) site within the M_2Pn_2 slab is occupied by 42.7% Cr and 57.3% Mn, and the magnetic moments order antiferromagnetically below $T_N(M2)$ = 540 K with a C-type antiferromagnetic structure. The M(1) site within the MO_2 layers is fully occupied by Cr, and antiferromagnetic order is observed below $T_N(M1)$ = 200 K. Along *c*, there are two possible interplanar arrangements: ferromagnetic with the (1/2, 1/2, 0) propagation vector and antiferromagnetic with the (1/2, 1/2, 1/2) propagation vector. Magnetic phase separation arises so that both propagation vectors are observed below 200 K. Such magnetic phase separation has not been previously observed in $Sr_2M_3As_2O_2$ phases (M = Cr, Mn) and shows that there are several competing magnetic structures present in these compounds.

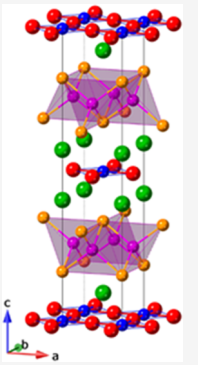

INTRODUCTION

Since the discovery of high-temperature superconductivity in iron oxyarsenides in 2006, layered pnictide compounds have seen increased research focus. Their superconductivity originates from the iron arsenide layers,[1] which are present in multiple structure types such as LiFeAs,[2] $SmFeAsO_{0.85}$,[3] $K_{0.8}Fe_2Se_2$,[4] $CaFe_2As_2$,[5] α-FeSe,[6] and (Fe_2As_2)-$[Ca_4(Sc,Ti)_3O_8]$.[7] It was soon discovered that upon substituting Fe for other transition metals, different phenomena emerge such as giant magnetoresistance in (La,Nd)MnAsO,[8] a spin reorientation transition in CeMnAsO,[9] colossal magnetoresistance in $NdMnAsO_{1-x}F_x$,[10] persistent short-range order above T_N in LaMnAsO,[11] p-type semiconductivity in LaCuChO (Ch = S, Se, Te),[12] and competing spin-density-wave magnetism and superconductivity in $EuFe_2As_2$.[13] Studying these materials could lead to advances in high-field applications and electronic data storage and open additional avenues to determine the exact mechanisms of unconventional superconductivity.

The oxyarsenides $A_2M_2M'As_2O_2$ (M and M' represent different transition metals) are especially interesting, as they contain key structural elements of both the iron arsenide and cuprate superconductors. These materials crystallize in the tetragonal crystal system, space group *I*4/*mmm*, and are composed of square planar $M(1)O_2$ layers and tetrahedral $M(2)_2As_2$ layers. These layers are stacked on top of each other perpendicular to the crystallographic *c* axis and are separated by layers of alkali-earth cations (A^{2+}). Several oxyarsenides, specifically $A_2M_{3-x}M'_xAs_2O_2$ (A = Ba, Sr; M_x = Mn_3,[14] Cr_3,[15−17] $Cr_{0.77}Mn_{2.23}$,[18] $MnZn_2$,[19,20] Mn_2Cu,[19] Zn_3[21]), have been synthesized and investigated. While $Sr_2Fe_2CuAs_2O_2$ should be the most interesting compound to study, being composed of the cuprate (CuO_2) and iron-based (Fe_2As_2) superconductor superconducting layers, it was reported that syntheses did not yield a single-phase product.[19] However, it was discovered that CrAs becomes superconducting under pressure as the antiferromagnetic ordering is quenched[22] and that superconductivity could potentially be induced in $Sr_2Cr_3As_2O_2$, either with pressure or with chemical doping.[17] It was also determined that MnP becomes superconducting at ∼8 GPa.[23] This prompted our exploration of compounds within the series $Sr_2Cr_{3-x}Mn_xAs_2O_2$.

Very different magnetic structures have been reported for $Sr_2Mn_3As_2O_2$,[14,19] $Sr_2Cr_3As_2O_2$,[16] and $Sr_2Cr_{0.77}Mn_{2.23}As_2O_2$.[18] $Sr_2Cr_3As_2O_2$ exhibits antiferromagnetic ordering of the M(2) sites below 590.3 K, with the propagation vector k = (1, 0, 0), and the moments aligned parallel to the *c* axis. Below 291 K, the M(1) sites order antiferromagnetically, with a K_2NiF_4-type antiferromagnetic structure and propagation vector k = (1/2, 1/2, 0) (moments aligned parallel to *c*), which causes a spin-flop of the M(2) spins onto the *ab* plane.[16] The $Sr_2Mn_3As_2O_2$ compound exhibits G-type antiferromagnetic ordering with the propagation vector k = 0 of the M(2) sites below 340 K with spins aligned parallel to the *c* axis and short-range two-dimensional magnetic correlations below 75 K so that the M(1) sublattice does not exhibit long-range magnetic order down to 4 K. Additional peaks were observed at 4 K but could not be satisfactorily modeled.[14,19] The mixed transition-metal compound $Sr_2Cr_{0.77}Mn_{2.23}As_2O_2$ exhibits G-type antiferromag-

Received: March 18, 2022
Published: August 4, 2022

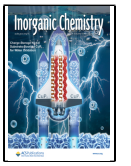

netic ordering of the M(2) sites with k = 0 between 410 and 167 K (with moments along the *c* axis), and antiferromagnetic ordering of the M(1) sites below 167 K (moments along the *c* axis) with k = (1/2, 1/2, 0), which causes a reorientation of the M(2) moments to a C-type antiferromagnetic arrangement (moments along the *c* axis) with k = (1, 0, 0).[18]

The magnetic transition temperatures in these compounds are also affected by the transition-metal stoichiometry with T_N decreasing as the Cr:Mn ratio decreases.[19] Xu et al.[15] have recently discussed the interlayer coupling of magnetic sublattices in $Sr_2Cr_3As_2O_2$, prompted by their observation of a spin-flop transition of the M(2) site magnetic moments upon the emergence of long-range order of the M(1) site moments, which was also reported by Liu et al.[16] A similar (field-induced) phenomenon has also recently been observed in $EuMnBi_2$[24] and coupling of the magnetic sublattices has been observed in the 1111-type compounds such as SmFeAsO,[25] CeMnAsO,[26] and PrMnSbO.[27] However, in these examples, both magnetic sublattices have the same propagation vector. The coupling of magnetic lattices with different propagation vectors should not occur in principle; however, it seems that $A_2M_2M'As_2O_2$ oxypnictides exhibit this phenomenon.[15] The spin reorientation and magnetic coupling were attributed to an antisymmetric exchange (Dzyaloshinskii−Moriya interaction), however, no significant accompanying structural distortion could be determined.[15]

Since we have observed a similar spin-flip transition in $Sr_2Cr_{0.77}Mn_{2.23}As_2O_2$,[18] we have started to explore the magnetic structures of other members of this solid solution series to better understand the interactions between the layers. We have now synthesized $Sr_2Cr_2MnAs_2O_2$, and here we report the crystal structure and changes in the magnetic structure with temperature.

EXPERIMENTAL SECTION

A polycrystalline sample of the nominal stoichiometry $Sr_2Cr_2MnAs_2O_2$ was prepared using a standard solid-state synthesis on a 1.2 g scale. The starting materials used were Mn (99.99%, Aldrich), Cr (≥99%, Aldrich), As (99.999%, Aldrich), and $SrCO_3$ (99.9 + %, Aldrich). SrO was prepared by heating $SrCO_3$ at 1250 °C for 12 h, followed by quenching and immediate use. Stoichiometric amounts of Mn, Cr, and As were mixed with a nonstoichiometric amount of SrO (2% deficiency). In agreement with the reported syntheses of $Sr_2Cr_3As_2O_2$[16,17] and $Sr_2Cr_{0.77}Mn_{2.23}As_2O_2$,[18] we have observed that the deficiency increased phase purity. All starting materials were mixed and ground in an inert atmosphere (N_2, UN1066 BOC) environment using an agate mortar and pestle. The mixture was pelleted and inserted into a Ta crucible (foil 0.05 mm, ≥99.9%, Aldrich), which was sealed in a quartz tube under vacuum. The pellets were heated at 1080 °C for 72 h twice, with intermediate regrinding.

Room-temperature powder X-ray diffraction was performed on a PANalytical Empyrean Powder diffractometer. Patterns were recorded using Cu Kα1 radiation, in the range of 5° < 2θ < 100°, with a step size of 0.01313°.

Variable temperature neutron diffraction experiments were performed on the D1B and D2B diffractometers at the Institut Laue-Langevin in Grenoble, France (ILL). Approximately, 1.5 g of the sample powder was inserted into a 9 mm vanadium can. Data were recorded on the D1B diffractometer with λ = 2.512 Å, with a temperature range of 1.5−420 K upon heating at the rate of 1 K/170 s and 375−673 K on heating at the rate of 1 K/200 s, separated into 600 s snapshots (3.5−3 K range, respectively). Further patterns were recorded on the D2B diffractometer with λ = 1.594 Å at 1.5, 50, 100, 150, 200, 250, 300, 350, 400, 450, 500, and 600 K. Data were collected for 2.5 h at each temperature step.

The temperature dependence of the magnetic susceptibility was performed with a Quantum Design Superconducting Quantum Interference Device (SQUID) magnetometer. Field-cooled (FC) and zero-field-cooled (ZFC) measurements were recorded in a field of 1000 Oe between 4 and 340 K. The temperature dependence of the electrical resistance was performed with a Quantum Design physical property measurement system (PPMS). Measurements were recorded on heating between 4 and 340 K.

RESULTS AND DISCUSSION

$Sr_2Cr_2MnAs_2O_2$ crystallizes in the tetragonal crystal system with the space group *I*4/*mmm*. The unit cell of $Sr_2Cr_2MnAs_2O_2$ is composed of $M(1)O_2$ planes and $M(2)_2As_2$ layers, separated by Sr^{2+} ions, as shown in Figure 1. Initial structural analysis was performed using Rietveld

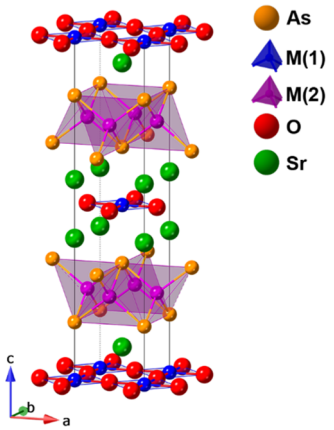

Figure 1. Crystal structure of $Sr_2Cr_{1.85}Mn_{1.15}As_2O_2$ showing the alternating M(1) CuO_2-type and M(2) FeAs-type layers along *c*.

refinement on laboratory X-ray powder diffraction patterns. These were refined using a model of the $Sr_2Cr_3As_2O_2$ crystal cell,[15−17] modified to $Sr_2Cr_2MnAs_2O_2$ by replacing half of the M(2) site Cr occupancy with Mn. The patterns could be indexed well on the tetragonal unit cell, with cell parameters *a* = 4.0428(1) Å and *c* = 18.9578(6) Å. A small impurity phase of $Sr_2Cr_2AsO_3$ is observed and fitted (0.7% by mass). This impurity has previously been identified by Xu et al. during the synthesis of $Sr_2Cr_3As_2O_2$.[15]

The M(1) and M(2) transition-metal sites, located at Wyckoff positions 2a and 4d, respectively, have different local environments. The M(1) sites are in square planar or, arguably, distended octahedral coordination,[15] and the M(2) sites are in tetrahedral coordination. Powder neutron diffraction data were recorded to determine site occupancies and magnetic ordering of $Sr_2Cr_2MnAs_2O_2$. Rietveld refinement was first performed on the *I*4/*mmm* model with the GSAS/EXPGUI[28,29] software using the high-resolution diffraction pattern obtained at *T* = 600 K (Figure 2a), where no magnetic peaks were observed. The background was fitted using the Chebyshev polynomial function with 15 terms and the peaks were fitted using the pseudo-Voigt profile function. An excellent fit was obtained using the *I*4/*mmm* space group with *a* = 4.06066(4) Å and *c* = 19.1220(4) Å (χ^2 = 2.91). The atomic displacement parameters were modeled isotopically with the U_{iso}s for Cr and Mn constrained to the same value. Site occupancies were refined for all atoms and fixed to 1.0 where the refined values were within ±1% of the full occupancy. It was determined that the M(1) site is fully

https://doi.org/10.1021/acs.inorgchem.2c00885
Inorg. Chem. 2022, 61, 12518−12525

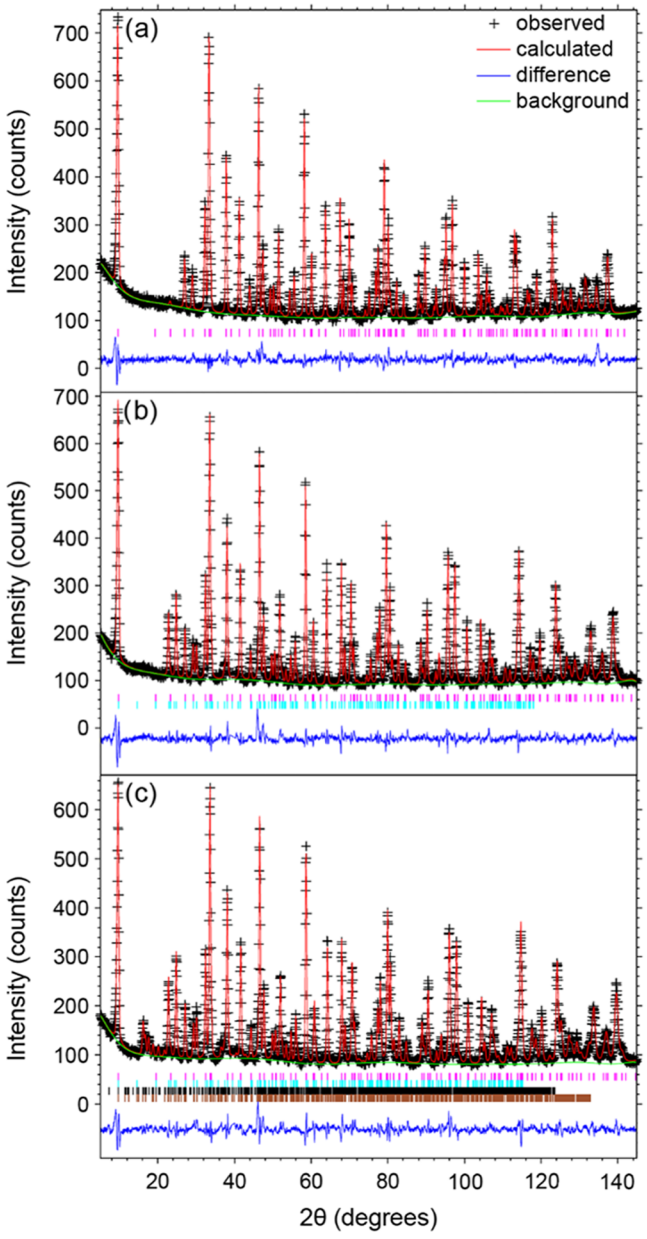

Figure 2. Rietveld refinements against high-resolution neutron diffraction patterns of $Sr_2Cr_{1.85}Mn_{1.15}As_2O_2$ at (a) T = 600 K, (b) 300 K, and (c) 1.5 K. The violet, cyan, brown, and black ticks represent the possible reflections of the nuclear, k_1 = (1, 0, 0), k_2 = (1/2, 1/2, 0), and k_3 = (1/2, 1/2, 1/2) magnetic phases, respectively. The patterns were recorded on the D2B diffractometer with λ = 1.594 Å. The agreement factors from Rietveld fits are shown in Table S1.

occupied by Cr, while the M(2) site is occupied by 42.7(4)% Cr and 57.3(4)% Mn. These values were used, with no further refinement, at all temperatures. This distribution was attributed to the effects of crystal field stabilization energy and Jahn–Teller distortion, as previously reported for $Sr_2Mn_{2.23}Cr_{0.77}As_2O_2$.[18] The Cr^{2+} ion favors octahedral and square planar coordination[30] and fills completely the square planar M(1) site. In contrast, the Mn^{2+} ion displays no site selectivity and is therefore found at the M(2) site. This is also observed in $A_2MnZn_2As_2O_2$ (A = Sr, Ba), where the Mn^{2+} ions occupy the M(1) site and the Zn^{2+} ions occupy the M(2) site,[31] due to the tetrahedral site preference[30] of Zn^{2+}. Additional Rietveld refinements against selected patterns are shown in Figures 2 and S1, and the refined atomic parameters, cell parameters, and agreement factors from Rietveld fits are shown in Table S1.

Rietveld refinement shows that the stoichiometry is $Sr_2Cr_{1.85}Mn_{1.15}As_2O_2$ so that, like $Sr_2Cr_{0.77}Mn_{2.23}As_2O_2$,[18] the final synthesized compound contains less Cr than expected. The unit cell parameters exhibit normal thermal expansion (Figure S2). Due to the anisotropic shape of the unit cell, thermal expansion favors the c axis. The unit cell therefore elongates slightly with increasing temperature, and the c/a ratio changes from 4.68316(2) at 1.5 K to 4.70907(2) at 600 K (Table S1). The M(2)–As and Cr–O bond lengths are shown in Figure S3. Both bond lengths increase upon heating, while the As–M(2)–As angles do not change significantly (Table S2). There is also no evidence of magnetostriction at any temperature.

High-intensity neutron diffraction data collected on the D1B diffractometer during continuous sample heating were used to determine the onset of magnetic ordering. Additional peaks were observed below T_N(M2) = 540 K in both the D2B data (Figure 3) and D1B data (Figure 4). These peaks could be

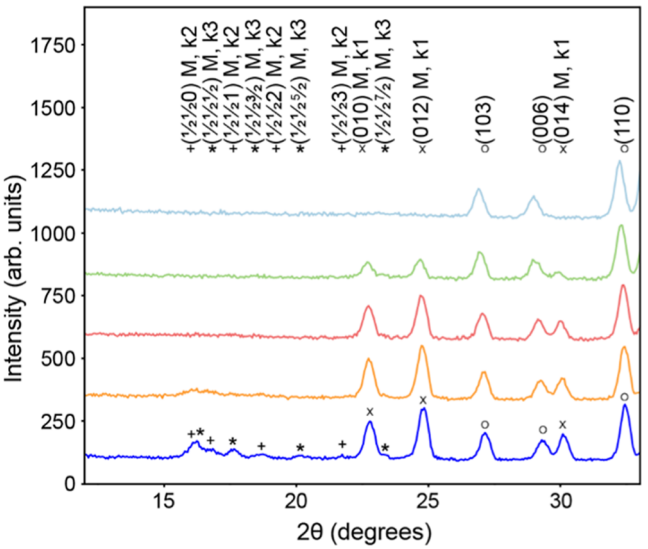

Figure 3. High-resolution neutron diffraction patterns at 1.5, 200, 300, 500, and 600 K (bottom to top) recorded on the D2B diffractometer with λ = 1.594 Å. The gradual appearance of magnetic diffraction peaks with a decreasing temperature is observed. The *hkl*s are marked with x, +, *, and o, for the magnetic phases with the propagation vectors k_1 = (1, 0, 0), k_2 = (1/2, 1/2, 0), k_3 = (1/2, 1/2, 1/2), and the nuclear phase, respectively.

indexed with the propagation vector k_1 = (1, 0, 0), which corresponds to a C-type antiferromagnetic arrangement of the M(2) spins with spins aligned parallel to the c axis. This magnetic structure is the same as that previously reported for $Sr_2Cr_{0.77}Mn_{2.23}As_2O_2$[18] at a low temperature (Figure 5a). Below 290 K, further additional broad peaks are observed (Figures 4 and S4). Such peaks are reminiscent of short-range magnetic correlations, as observed in $Sr_2Mn_3As_2O_2$ below 75 K,[14] in $Ba_2Zn_2MnAs_2O_2$ below 30 K,[31] and in the pnictide layer of LaMnAsO from 360 (1) to 650 (10) K.[11] Upon cooling below 200 K (T_N(M1)), sharper magnetic peaks are observed, which could be indexed by two propagation vectors. The magnetic peaks can be indexed by k_2 = (1/2, 1/2, 0), which corresponds to a K_2NiF_4-type antiferromagnetic

https://doi.org/10.1021/acs.inorgchem.2c00885
Inorg. Chem. 2022, 61, 12518–12525

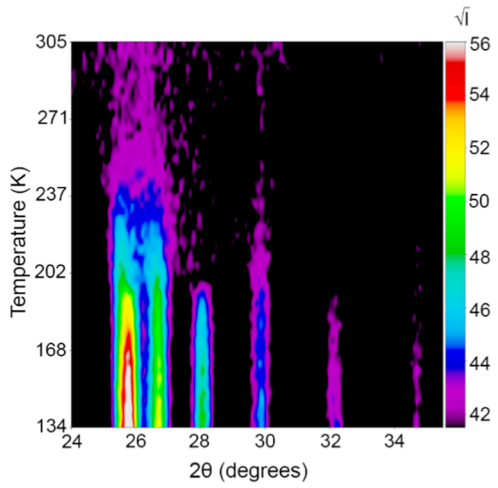

Figure 4. Contour plot of high-intensity data recorded on the D1B diffractometer. Data were recorded on the D1B diffractometer with λ = 2.512 Å. The intensities are presented as $\sqrt{I}$. Broad magnetic peaks are observed between 200 and 290 K, as the ordering shifts from a long range to a short range before disappearing entirely. The peaks at 28 and 32° two thetas correspond to k_3 = (1/2, 1/2, 1/2).

structure of the M(1) site magnetic moments with moments ordered parallel to the *c* axis, as shown in Figure 5b. The magnetic peaks can also be indexed with the propagation vector k_3 = (1/2, 1/2, 1/2) (Figures 3 and 4). The moments remain aligned parallel to the *c* axis, and the magnetic structure for this propagation vector is shown in Figure 5c. There is no change in the magnetic structure of the $M(2)_2As_2$ layer upon further cooling.

The moments on the M(1) site order with a K_2NiF_4-type magnetic structure. The intraplanar (*ab* plane) ordering of the magnetic moments is antiferromagnetic. Due to the body-centered tetragonal crystal structure of the compound, the coupling of the nearest neighboring MO_2 layers' magnetic moments is a net zero, as each atom has an equal number of ferro- and antiferromagnetically aligned neighbors. The interlayer coupling thus occurs between the next nearest neighboring (nnn) layers, which is favorable in these materials.[31] Along *c*, there are two possible nnn interplanar arrangements: ferromagnetic with a propagation vector of (1/2, 1/2, 0) (Figure 5b) and antiferromagnetic with a propagation vector of (1/2, 1/2, 1/2) (Figure 5c).

Below 200 K, a successful fit to the experimental data was achieved with a model containing 46(4)% k_2 = (1/2, 1/2, 0) (Figure 5b) and 54(5)% k_3 = (1/2, 1/2, 1/2) (Figure 5c), with the k_3 and k_2 moments' magnitudes constrained so that $\sqrt{2}|m_{k3}| = |m_{k2}|$. Hence, magnetic phase segregation is observed below 200 K. The phase fraction distribution gradually changes to 29(2)% k_2 = (1/2, 1/2, 0) and 71(4)% k_3 = (1/2, 1/2, 1/2) at 168 K, with no further changes down to the lowest temperature measured. During refinement, the fractions of both phases were constrained with the assumption that the entire volume of the sample exhibits ordering of the M(1) site moments. Due to the unstable nature of refining both the magnitudes and the fractions of the separate phases concurrently, they were refined separately, iterating between

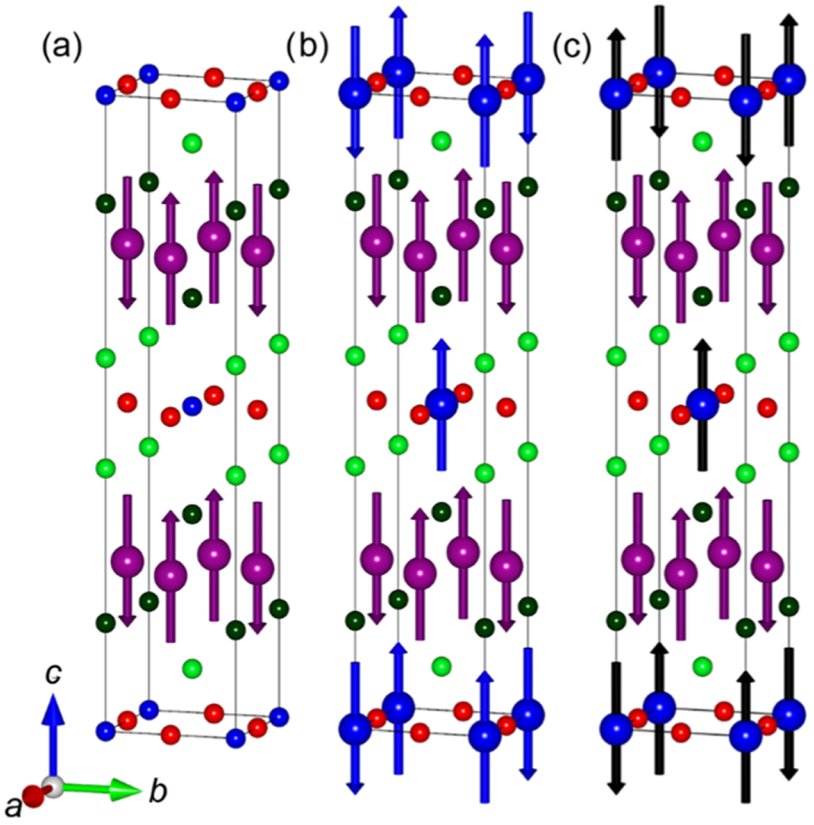

Figure 5. Magnetic structures of $Sr_2Cr_{1.85}Mn_{1.15}As_2O_2$ below T_N(M2) = 540 K (a) and below T_N(M1) = 200 K (b, c). Below 200 K, all three magnetic structures are observed, with the M(1) magnetic structures depicted in (b, c) in competition. The k_1 = (1, 0, 0), k_2 = (1/2, 1/2, 0), and k_3 = (1/2, 1/2, 1/2) magnetic moments are represented by violet, blue, and black arrows, respectively.

https://doi.org/10.1021/acs.inorgchem.2c00885
Inorg. Chem. 2022, 61, 12518−12525

refining moments and scales in several steps until sufficient convergence was achieved.

The variation of the M(1) and M(2) site magnetic moments of $Sr_2Cr_{1.85}Mn_{1.15}As_2O_2$ with temperature is shown in Figure 6.

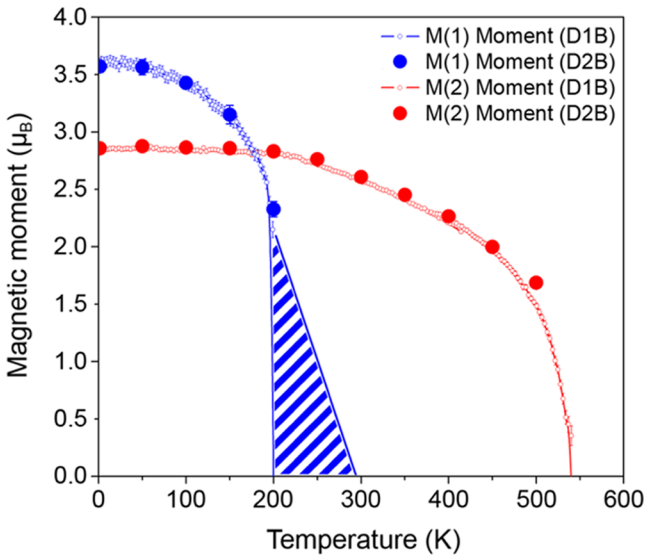

Figure 6. Variation of the M(1) and M(2) site magnetic moments with temperature. The smaller open symbols represent high-intensity D1B data, while the larger closed symbols represent high-resolution D2B data. The red curve represents the M(2) moments below $T_N(M2)$ = 540 K. Below $T_N(M1)$ = 200 K, the blue curve represents the M(1) moments belonging to both the magnetic phases with k_2 = (1/2, 1/2, 0) and k_3 = (1/2, 1/2, 1/2). The moment magnitudes were constrained as $\sqrt{2}|m_{k3}| = |m_{k2}|$. The blue striped area (200 K < T < 290 K) is an approximation of the M(1) moments where short-range magnetic order is observed.

Short-range magnetic order of the M(2) moments is detected below 290 K. At 200 K, the M(1) moments order antiferromagnetically and magnetic phase separation is observed. Magnetic phase separation occurs when there is competition between magnetic ground states. Examples include the colossal magnetoresistant manganite perovskites where chemical doping on the Mn site results in competition between a charge/orbital-ordered antiferromagnetic phase and a ferromagnetic metallic phase[32] and $Ca_3(Ru_{1-x}Ti_x)_2O_7$ where two competing antiferromagnetic phases are observed in a narrow doping range (x = 0.02−0.05).[33] Such magnetic phase separation has not been previously observed in $Sr_2M_3As_2O_2$ phases (M = Cr, Mn). It has been established that the intraplanar coupling constant is several orders of magnitude greater than the interlayer coupling constant, due to the long interlayer distance in these compounds. As such, interlayer coupling occurs once the correlation length within the layers reaches a sufficient length.[34] The exchange energies for nnn layer ferromagnetic and antiferromagnetic alignment along c at the M(1) site would appear to be almost equivalent in this compound so that there are competing spin structures and two propagation vectors observed below $T_N(M1)$. Similar magnetic phase separation has previously been reported for $RuSr_2Y_{1.5}Ce_{0.5}Cu_2O_{10-\delta}$[35] and Rb_2MnF_4.[36]

At 1.5 K, the saturated magnetic moments of the M(2) and M(1) sites are 2.86(2) and 3.57(5) μ_B, respectively. It has previously been shown that there is a correlation between T_N at both the M(1) and M(2) sites with the Mn(1)−O and the Mn(2)−Mn(2) distances in $A_2Mn_3Pn_2O_2$ (A = Sr, Ba; Pn = P, As, Sb);[32] both magnetic ordering temperatures increase as the a cell parameter decreases as a result of increasing superexchange (M(1)−O−M(1) and M(2)−As−M(2)) and direct exchange (M(2)−M(2)) interactions in the $M(1)-O_2$ and $M(2)_2As_2$ layers. Figure S5 shows that as x is increased in the $Sr_2Cr_{3-x}Mn_xAs_2O_2$ solid solution, there is a linear increase in the cell volume. As a result, there is a clear reduction in the antiferromagnetic ordering temperature at both the M(1) and M(2) sites as x increases (Figure 7). This results in a lower T_N

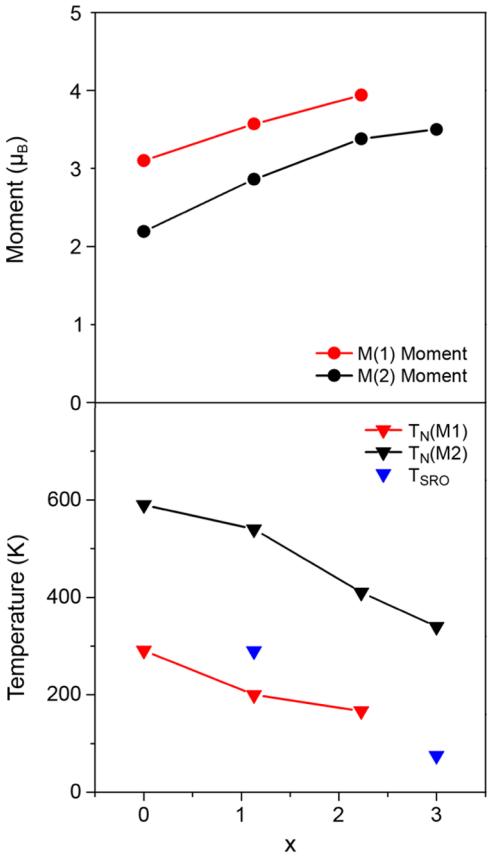

Figure 7. Variation of the magnetic moment magnitudes at 4 K (top) and ordering temperatures (bottom) with x in $Sr_2Cr_{3-x}Mn_xAs_2O_2$. The magnitudes of the moments at 4 K are represented by red (M(1) site) and black (M(2) site) circles. The ordering temperatures are represented by the red and black triangle marks for the long-range order of the M(1) and M(2) site magnetic moments, respectively. The blue triangle marks represent the temperatures below which the short-range order of the M(1) site magnetic moments is observed. The short-range order is observed between 290 and 200 K in $Sr_2Cr_{1.85}Mn_{1.15}As_2O_2$ and below 75 K down to the lowest temperature measured in $Sr_2Mn_3As_2O_2$.

in $Sr_2Cr_{1.85}Mn_{1.15}As_2O_2$ compared to $Sr_2Cr_3As_2O_2$, despite both compounds having the same $M(1)O_2$ layer composition (CrO_2). While the T_N in these compounds differs, the observed short-range magnetic order in $Sr_2Cr_{1.85}Mn_{1.15}As_2O_2$ emerges at a similar temperature (~290 K), as the long-range magnetic order in $Sr_2Cr_3As_2O_2$ (291 K). As the cell volume then decreases to 309.194(7) Å^3 at 200 K, the correlation length in the CrO_2 layers in $Sr_2Cr_{1.85}Mn_{1.15}As_2O_2$ reaches a sufficient length for the long-range order to be established.

Due to the partially covalent nature of the M−As and M−O bonds, the magnitudes of the saturated magnetic moments are

https://doi.org/10.1021/acs.inorgchem.2c00885
Inorg. Chem. 2022, 61, 12518−12525

lower than the theoretical values for Cr^{2+} and Mn^{2+} (4 and 5 μ_B, respectively) in all members of the series. However, the magnitudes of the M(2) and M(1) site moments both rise as the Mn^{2+} occupancy increases. The magnitude of the M(1)- and M(2)-ordered moments increases almost linearly with x in $Sr_2Cr_{3-x}Mn_xAs_2O_2$, for $0 \leq x \leq 2.23$ so that there does not seem to be any effect of Mn^{2+}/Cr^{2+} disorder on the overall ordered moment. The results suggest that the M(2) site moment magnitude is directly dependent on the composition of the layer, as the magnitude increases in proportion to the concentration of Mn^{2+} in the $M(2)_2As_2$ layer. The M(1) moment also increases linearly with x, which is surprising given that there is no change in the $M(1)O_2$ layer composition from $x = 0-1.15$. This increase in the M(1) moment could be a result of the reduction in covalency as the M(1)−O bond length increases across the series.

The magnetic structures reported so far for the $Sr_2Cr_{3-x}Mn_xAs_2O_2$ series are all different.[14,15,18] $Sr_2Cr_3As_2O_2$ and $Sr_2Cr_{1.85}Mn_{1.15}As_2O_2$ both exhibit C-type antiferromagnetic order in the $M(2)_2As_2$ layer below $T_N(M2)$, whereas G-type antiferromagnetic order is observed for $Sr_2Mn_{2.23}Cr_{0.77}As_2O_2$ and $Sr_2Mn_3As_2O_2$. This would suggest that the presence of Cr in the $M(2)_2As_2$ layer results in ferromagnetic interactions along c. As the order is established on the M(1) site below $T_N(M1)$, different magnetic structures are observed. In $Sr_2Cr_3As_2O_2$, the ordering of the M(1) site moments causes a spin-flop of the M(2) site moments.[15] In $Sr_2Cr_{0.77}Mn_{2.23}As_2O_2$, the ordering of the M(1) moments is followed by a spin-flip of the M(2) moments, shifting the antiferromagnetic ordering from G-type to C-type. In $Sr_2Cr_{1.85}Mn_{1.15}As_2O_2$, there is no evidence of a spin-flip or -flop so there does not appear to be any coupling of the M(1) and M(2) spins. This could be driven by the sizeable cation disorder in the $M(2)_2As_2$ layer, but further research is warranted. In contrast to other members of the series, magnetic phase segregation is observed in $Sr_2Cr_{1.85}Mn_{1.15}As_2O_2$ below 200 K and the two phases remain in competition down to the lowest measured temperature.

The temperature variation of the magnetic susceptibility of $Sr_2Cr_{1.85}Mn_{1.15}As_2O_2$ is presented in Figure 8. The reduction in susceptibility upon cooling is a signature of the antiferromagnetic transition in the $M(2)_2As_2$ layer at $T_N(M2) = 540$ K. There is no evidence of any further magnetic transitions in the susceptibility. The low-temperature magnetic transition in $Sr_2Cr_{0.77}Mn_{2.23}As_2O_2$ was also not evident in the magnetic susceptibility data.[18] There is no divergence between the FC and ZFC susceptibilities, and the upturn in the susceptibility below $T \approx 100$ K is attributed to paramagnetic impurity spins.

The thermal variation of the electrical resistivity of $Sr_2Cr_{1.85}Mn_{1.15}As_2O_2$ is presented in Figure 9 and exhibits semiconducting behavior. The 290 K resistivity is $7.769(5) \times 10^{-4}$ Ω cm, which is suggestive of a highly doped semiconductor verging on metallic behavior. The resistivity can be fit to the Arrhenius equation between 120 and 225 K giving a band gap of 2.85 meV. The electronic properties of the $A_2M_2M'As_2O_2$ compounds are dictated by the $M(2)_2As_2$ layers.[17,18] Cr_2As_2 layers exhibit metallic conductivity,[17] while Mn_2As_2 layers exhibit semiconducting behavior.[18] In the case of $Sr_2Cr_{1.85}Mn_{1.15}As_2O_2$, the $M(2)_2As_2$ layers are composed of $Mn_{1.15}Cr_{0.85}As_2$ and its resistivity exhibits a highly doped semiconductor-like temperature dependence. The conductivity of the $Sr_2Cr_{3-x}Mn_xAs_2O_2$ phases increases as the percentage of Cr on the M(2) site rises[17,18] so that the electronic properties can be tuned by varying the ratio of Cr:Mn on the M(2) site.

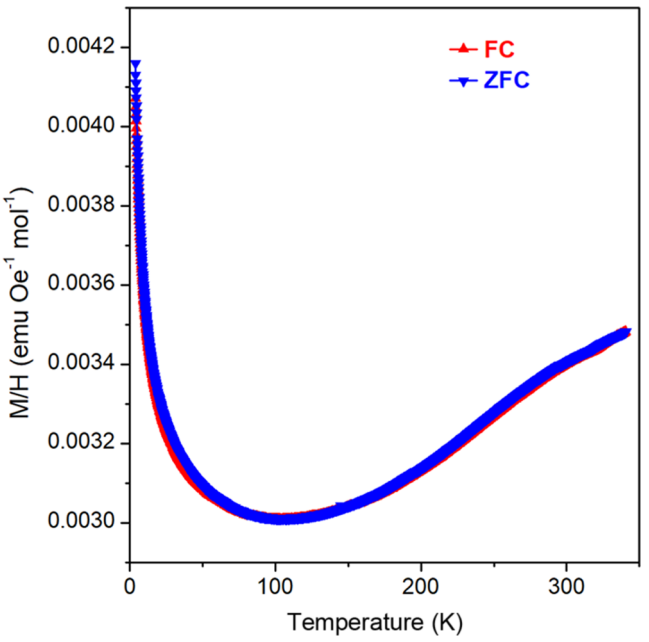

Figure 8. Temperature variation of the field-cooled and zero-field-cooled (FC and ZFC) susceptibility of $Sr_2Cr_{1.85}Mn_{1.15}As_2O_2$ (H = 1000 Oe).

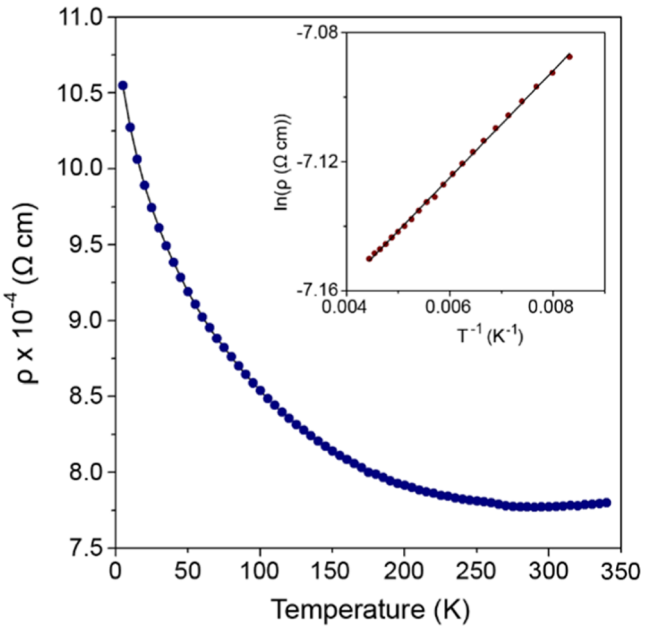

Figure 9. Temperature dependence of the electrical resistivity for $Sr_2Cr_{1.85}Mn_{1.15}As_2O_2$. The inset shows the fit to the Arrhenius equation between 120 and 225 K.

CONCLUSIONS

We have synthesized and analyzed the crystal and magnetic structures of $Sr_2Cr_{1.85}Mn_{1.15}As_2O_2$, which is the fourth member of the $Sr_2Cr_{3-x}Mn_xAs_2O_2$ solid solution. The magnetic properties are distinct from the other members of the series. In $Sr_2Cr_{1.85}Mn_{1.15}As_2O_2$, below $T_N(M1)$, magnetic phase separation is observed so that the M(1) moments order with the propagation vectors $k_2 = (1/2, 1/2, 0)$ and $k_3 = (1/2, 1/2,$

https://doi.org/10.1021/acs.inorgchem.2c00885
Inorg. Chem. 2022, 61, 12518−12525

1/2). The two phases remain in competition down to the lowest measured temperature. The competing spin structures arise as the exchange energies for nnn layer ferromagnetic and antiferromagnetic alignment at the M(1) site along *c* are almost equivalent in this compound. The results show that it is possible to tune the magnetic transition temperatures and magnetic structures by doping on the Cr site in $Sr_2Cr_{3-x}Mn_xAs_2O_2$. Substitution of Sr^{2+} for Ca^{2+} and Ba^{2+} or a variable temperature neutron diffraction at high pressure could provide further insight into the effects of interlayer distances and cell size on magnetic ordering in the $Sr_2Cr_{3-x}Mn_xAs_2O_2$ compounds.

■ ASSOCIATED CONTENT

Supporting Information

The Supporting Information is available free of charge at https://pubs.acs.org/doi/10.1021/acs.inorgchem.2c00885.

It includes figures showing Rietveld refinement fits, temperature variation of cell parameters and selected bond lengths, and tables of crystallographic data (PDF)

Accession Codes

CCDC 2163344 contains the supplementary crystallographic data for this paper. These data can be obtained free of charge via www.ccdc.cam.ac.uk/data_request/cif, or by emailing data_request@ccdc.cam.ac.uk, or by contacting The Cambridge Crystallographic Data Centre, 12 Union Road, Cambridge CB2 1EZ, UK; fax: +44 1223 336033.

■ AUTHOR INFORMATION

Corresponding Author

Abbie C. Mclaughlin − *The Chemistry Department, University of Aberdeen, Aberdeen AB24 3UE, Scotland; Institut Laue-Langevin, 71 Avenue des Martyrs, 38042 Grenoble, France; ISIS, Science and Technology Facilities Council, Rutherford Appleton Laboratory, Didcot OX11 0QX, U. K.;* orcid.org/0000-0001-9960-723X; Email: a.c.mclaughlin@abdn.ac.uk

Authors

Bor Arah − *The Chemistry Department, University of Aberdeen, Aberdeen AB24 3UE, Scotland*

Clemens Ritter − *Institut Laue-Langevin, 71 Avenue des Martyrs, 38042 Grenoble, France*

Gavin B. G. Stenning − *ISIS, Science and Technology Facilities Council, Rutherford Appleton Laboratory, Didcot OX11 0QX, U. K.*

Complete contact information is available at: https://pubs.acs.org/10.1021/acs.inorgchem.2c00885

Notes

The authors declare no competing financial interest.

■ ACKNOWLEDGMENTS

The authors thank the U.K. Science and Technology Facilities Council (STFC) for provision of neutron beamtime at the ILL under the experiment code 5-31-2665. Data are available from ILL at DOI:10.5291/ILL-DATA.5-31-2665.

■ REFERENCES

(1) Ozawa, T. C.; Kauzlarich, S. M. Chemistry of Layered *d*-Metal Pnictide Oxides and Their Potential as Candidates for New Superconductors. *Sci. Technol. Adv. Mater.* **2008**, *9*, No. 033003.

(2) Tapp, J. H.; Tang, Z.; Lv, B.; Sasmal, K.; Lorenz, B.; Chu, P. C. W.; Guloy, A. M. LiFeAs: An Intrinsic FeAs-Based Superconductor with T_c = 18 K. *Phys. Rev. B* **2008**, *78*, No. 060505.

(3) Ren, Z.-A.; Che, G.-C.; Dong, X.-L.; Yang, J.; Lu, W.; Yi, W.; Shen, X.-L.; Li, Z.-C.; Sun, L.-L.; Zhou, F.; Zhao, Z.-X. Superconductivity and Phase Diagram in the Iron-Based Arsenic-Oxides $ReFeAsO_{1-Delta}$ (Re = Rare Earth Metal) without F-Doping. *Europhys. Lett.* **2008**, *83*, No. 17002.

(4) Guo, J.; Jin, S.; Wang, G.; Wang, S.; Zhu, K.; Zhou, T.; He, M.; Chen, X. Superconductivity in the Iron Selenide KFe_2Se_2 ($0 \geq x \geq 1.0$). *Phys. Rev. B* **2010**, *82*, No. 180520.

(5) Kudo, K.; Iba, K.; Takasuga, M.; Kitahama, Y.; Matsumura, J. I.; Danura, M.; Nogami, Y.; Nohara, M. Emergence of Superconductivity at 45 K by Lanthanum and Phosphorus Co-Doping of $CaFe_2As_2$. *Sci. Rep.* **2013**, *3*, No. 1478.

(6) Hsu, F. C.; Luo, J. Y.; Yeh, K. W.; Chen, T. K.; Huang, T. W.; Wu, P. M.; Lee, Y. C.; Huang, Y. L.; Chu, Y. Y.; Yan, D. C.; Wu, M. K. Superconductivity in the PbO-Type Structure α-FeSe. *Proc. Natl. Acad. Sci. U.S.A.* **2008**, *105*, 14262−14264.

(7) Ogino, H.; Sato, S.; Kishio, K.; Shimoyama, J. I.; Tohei, T.; Ikuhara, Y. Homologous Series of Iron Pnictide Oxide Superconductors (Fe_2As_2) $[Ca_{n+1}(Sc,Ti)NO_y]$ (N = 3, 4, 5) with Extremely Thick Blocking Layers. *Appl. Phys. Lett.* **2010**, *97*, No. 072506.

(8) Emery, N.; Wildman, E. J.; Skakle, J. M. S.; Giriat, G.; Smith, R. I.; McLaughlin, A. C. Giant Magnetoresistance in Oxypnictides (La,Nd)OMnAs. *Chem. Commun.* **2010**, *46*, 6777−6779.

(9) Tsukamoto, Y.; Okamoto, Y.; Matsuhira, K.; Whangbo, M. H.; Hiroi, Z. A Magnetic Transition Probed by the Ce Ion in Square-Lattice Antiferromagnet CeMnAsO. *J. Phys. Soc. Jpn.* **2011**, *80*, No. 094708.

(10) Wildman, E. J.; Skakle, J. M. S.; Emery, N.; McLaughlin, A. C. Colossal Magnetoresistance in Mn^{2+} Oxypnictides $NdMnAsO_{1-x}F_x$. *J. Am. Chem. Soc.* **2012**, *134*, 8766−8769.

(11) McGuire, M. A.; Garlea, V. O. Short- and Long-Range Magnetic Order in LaMnAsO. *Phys. Rev. B* **2016**, *93*, No. 054404.

(12) Hosono, H.; Yamamoto, A.; Hiramatsu, H.; Ma, Y. Recent Advances in Iron-Based Superconductors toward Applications. *Mater. Today* **2018**, *21*, 278−302.

(13) Zapf, S.; Dressel, M. Europium-Based Iron Pnictides: A Unique Laboratory for Magnetism, Superconductivity and Structural Effects. *Rep. Prog. Phys.* **2017**, *80*, No. 016501.

(14) Brock, S. L.; Raju, N. P.; Greedan, J. E.; Kauzlarich, S. M. The Magnetic Structures of the Mixed Layer Pnictide Oxide Compounds $Sr_2Mn_3Pn_2O_2$ (Pn = As, Sb). *J. Alloys Compd.* **1996**, *237*, 9−19.

(15) Xu, X.; Jones, M. A.; Cassidy, S. J.; Manuel, P.; Orlandi, F.; Batuk, M.; Hadermann, J.; Clarke, S. J. Magnetic Ordering in the Layered Cr(II) Oxide Arsenides $Sr_2CrO_2Cr_2As_2$ and $Ba_2CrO_2Cr_2As_2$. *Inorg. Chem.* **2020**, *59*, 15898−15912.

(16) Liu, J.; Wang, J.; Sheng, J.; Ye, F.; Taddei, K. M.; Fernandez-Baca, J. A.; Luo, W.; Sun, G. A.; Wang, Z. C.; Jiang, H.; Cao, G. H.; Bao, W. Neutron Diffraction Study on Magnetic Structures and Transitions in $Sr_2Cr_3As_2O_2$. *Phys. Rev. B* **2018**, *98*, No. 134416.

(17) Jiang, H.; Bao, J. K.; Zhai, H. F.; Tang, Z. T.; Sun, Y. L.; Liu, Y.; Wang, Z. C.; Bai, H.; Xu, Z. A.; Cao, G. H. Physical Properties and Electronic Structure of $Sr_2Cr_3As_2O_2$ Containing CrO_2 and Cr_2As_2 Square-Planar Lattices. *Phys. Rev. B* **2015**, *92*, No. 205107.

(18) Lawrence, G. B.; Wildman, E. J.; Stenning, G. B. G.; Ritter, C.; Fauth, F.; McLaughlin, A. C. Electronic and Magnetic Properties of Cation Ordered $Sr_2Mn_{2.23}Cr_{0.77}As_2O_2$. *Inorg. Chem.* **2020**, *11*, 7553−7560.

(19) Nath, R.; Garlea, V. O.; Goldman, A. I.; Johnston, D. C. Synthesis, Structure, and Properties of Tetragonal $Sr_2M_3As_2O_2$ (M_3 = Mn_3, Mn_2Cu, and $MnZn_2$) Compounds Containing Alternating CuO_2-Type and FeAs-Type Layers. *Phys. Rev. B* **2010**, *81*, No. 224513.

(20) Ozawa, T.; Olmstead, M. M.; Brock, S. L.; Kauzlarich, S. M.; Young, D. M. Synthesis and Characterization of a New Compound with Alternating MnO^{2-} and Zn_2As^{2-} Layers: $Ba_2MnZn_2As_2O_2$. *Chem. Mater.* **1998**, *10*, 392−396.

(21) Brock, S. L.; Kauzlarich, S. M. $A_2Zn_3As_2O_2$ (A = Ba, Sr): A Rare Example of Square Planar Zinc. *Inorg. Chem.* **1994**, *33*, 2491−2492.
(22) Wu, W.; Cheng, J.; Matsubayashi, K.; Kong, P.; Lin, F.; Jin, C.; Wang, N.; Uwatoko, Y.; Luo, J. Superconductivity in the Vicinity of Antiferromagnetic Order in CrAs. *Nat. Commun.* **2014**, *5*, No. 5508.
(23) Cheng, J. G.; Matsubayashi, K.; Wu, W.; Sun, J. P.; Lin, F. K.; Luo, J. L.; Uwatoko, Y. Pressure Induced Superconductivity on the Border of Magnetic Order in MnP. *Phys. Rev. Lett.* **2015**, *114*, No. 117001.
(24) Zhu, F.; Wang, X.; Meven, M.; Song, J.; Mueller, T.; Yi, C.; Ji, W.; Shi, Y.; Ma, J.; Schmalzl, K.; Schmidt, W. F.; Su, Y.; Brückel, T. Magnetic Structures, Spin-Flop Transition, and Coupling of Eu and Mn Magnetism in the Dirac Semimetal $EuMnBi_2$. *Phys. Rev. Res.* **2020**, *2*, No. 043100.
(25) Nandi, S.; Su, Y.; Xiao, Y.; Price, S.; Wang, X. F.; Chen, X. H.; Herrero-Martín, J.; Mazzoli, C.; Walker, H. C.; Paolasini, L.; Francoual, S.; Shukla, D. K.; Strempfer, J.; Chatterji, T.; Kumar, C. M. N.; Mittal, R.; Rønnow, H. M.; Rüegg, C.; McMorrow, D. F.; Brückel, T. Strong Coupling of Sm and Fe Magnetism in SmFeAsO as Revealed by Magnetic X-Ray Scattering. *Phys. Rev. B* **2011**, *84*, No. 054419.
(26) Corkett, A. J.; Free, D. G.; Clarke, S. J. Spin-Reorientation Transition in CeMnAsO. *Inorg. Chem.* **2015**, *54*, 1178−1184.
(27) Kimber, S. A. J.; Hill, A. H.; Zhang, Y. Z.; Jeschke, H. O.; Valentí, R.; Ritter, C.; Schellenberg, I.; Hermes, W.; Pöttgen, R.; Argyriou, D. N. Local Moments and Symmetry Breaking in Metallic PrMnSbO. *Phys. Rev. B* **2010**, *82*, No. 100412.
(28) Toby, B. H.EXPGUI, a graphical user interface for GSAS *J. Appl. Cryst.*, 2001; Vol. *34*, pp 210−213 https://subversion.xray.aps.anl.gov/trac/EXPGUI DOI: 10.1107/S0021889801002242.
(29) Larson, A. C.; Von Dreele, R. B."General Structure Analysis System (GSAS) *Los Alamos National Laboratory Report LAUR*, 2000, pp 86−748 https://subversion.xray.aps.anl.gov/trac/EXPGUI/wiki/GSASIntro.
(30) Waroquiers, D.; Gonze, X.; Rignanese, G. M.; Welker-Nieuwoudt, C.; Rosowski, F.; Göbel, M.; Schenk, S.; Degelmann, P.; André, R.; Glaum, R.; Hautier, G. Statistical Analysis of Coordination Environments in Oxides. *Chem. Mater.* **2017**, *29*, 8346−8360.
(31) Ozawa, T. C.; Kauzlarich, S. M.; Bieringer, M.; Wiebe, C. R.; Greedan, J. E.; Gardner, J. S. The Effect of Interlayer Cations on the Magnetic Properties of the Mixed-Metal Pnictide Oxides: $A_2MnZn_2As_2O_2$ (A = Sr, Ba). *Chem. Mater.* **2001**, *13*, 973−980.
(32) Dagotto, E.; Hotta, T.; Moreo, A. Colossal magnetoresistant materials: the key role of phase separation. *Phys. Rep.* **2001**, *344*, 1−153.
(33) Peng, J.; Liu, J. Y.; Hu, J.; Mao, Z. Q.; Zhang, F. M.; Wu, X. S. Magnetic phase separation in double layer ruthenates $Ca_3(Ru_{1-x}Ti_x)_2O_7$. *Sci. Rep.* **2016**, *6*, No. 19462.
(34) Brock, S. L.; Kauzlarich, S. M. Structure-Property Relationships in a Series of Mixed Layer Pnictide Oxide Compounds: $A_2Mn_3Pn_2O_2$ (A Sr, Ba; PnP, As, Sb). *J. Alloy Compd.* **1996**, *241*, 82−88.
(35) McLaughlin, A. C.; Felner, I.; Awana, V. P. S. Neutron Diffraction Study of the Magnetic Structure of the Superconducting Ru-1222-Type Ruthenocuprate $RuSr_2Y_{1.5}Ce_{0.5}Cu_2O_{10-\delta}$: Evidence for Long-Range Antiferromagnetic Order. *Phys. Rev. B* **2008**, *78*, No. 094501.
(36) Birgeneau, R. J.; Guggenheim, H. J.; Shirane, G. Neutron Scattering Investigation of Phase Transitions and Magnetic Correlations in the Two-Dimensional Antiferromagnets K_2NiF_4, Rb_2MnF_4, Rb_2FeF_4. *Phys. Rev. B* **1970**, *1*, 2211−2230.

https://doi.org/10.1021/acs.inorgchem.2c00885
Inorg. Chem. 2022, 61, 12518−12525